Title
Multistep inversion workflow for 3D long-offset damped elastic waves in the Fourier domain

Journal
Geophysical Prospecting, 65(5)

ISSN
0016-8025

Authors
Petrov, Petr V
Newman, Gregory A

Publication Date
2017-09-01

DOI
10.1111/1365-2478.12487

Peer reviewed

Multistep inversion workflow for 3D long-offset damped elastic waves in the Fourier domain

Petr V. Petrov

Gregory A. Newman
First published: 20 January 2017
https://doi.org/10.1111/1365-2478.12487
UC-eLinks

ABSTRACT

We present a new workflow for imaging damped three-dimensional elastic wavefields in the Fourier domain. The workflow employs a multiscale imaging approach, in which offset lengths are laddered, where frequency content and damping of the data are changed cyclically. Thus, the inversion process is launched using short-offset and low-frequency data to recover the long spatial wavelength of the image at a shallow depth. Increasing frequency and offset length leads to the recovery of the fine-scale features of the model at greater depths. For the fixed offset, we employ (in the imaging process) a few discrete frequencies with a set of Laplace damping parameters. The forward problem is solved with a finite-difference frequency-domain method based on a massively parallel iterative solver. The inversion code is based upon the solution of a least squares optimisation problem and is solved using a nonlinear gradient method. It is fully parallelised for distributed memory computational platforms. Our full-waveform inversion workflow is applied to the 3D Marmousi-2 and SEG/EAGE Salt models with long-offset data. The maximum inverted frequencies are 6 Hz for the Marmousi model and 2 Hz for the SEG/EAGE Salt model. The detailed structures are imaged successfully up to the depth approximately equal to one-third of the maximum offset length at a resolution consistent with the inverted frequencies.

INTRODUCTION

Three-dimensional full-waveform inversion (FWI) is an advanced seismic imaging technique that has recently become more computationally feasible and, thus, more frequently employed within the oil and gas industry (Plessix *et al*. 2010; Sirgue *et al*. 2010; Kapoor *et al*. 2013; Warner *et al*. 2013; Warner 2014). It is well known that FWI can be used to successfully update subsurface seismic attributes at relevant exploration depths, provided the acquired data contain a sufficient number of frequencies and long offsets. If the recording time is sufficient, the long offsets enable the reconstruction of the deepest parts of geological structures: long-offset data are primarily sensitive to turning waves, whose refraction depth covers the zone of interest. According to Ikelle (1995), the sensitivity of the inverted image depth is approximately from 0.5 to 0.7 of the offset. However, utilising long-range offsets requires additional efforts such as handling a wide range of wave types, processing wide-aperture datasets in an alternative manner,

and generating a sufficiently accurate background starting velocity model for FWI (Shipp and Singh 2002; Wang and Rao 2009). For computational reasons, most 3D applications still employ acoustic modelling assumptions, thereby neglecting elastic effects. Over the past few years, 3D acoustic FWI has been applied to several marine and terrestrial seismic datasets (Operto *et al*. 2007; Plessix *et al*. 2010; Sirgue *et al*. 2010; Vigh *et al*. 2010; Vigh, Kapoor and Li 2011).

Elastic FWI applications are mainly performed in 2D (e.g., Choi, Min and Shin 2008; Sears, Singh and Barton 2008; Brossier, Operto and Virieux 2009, 2015; Köhn *et al*. 2012). Unfortunately, the 2D approximation is unable to describe scattering effects arising from 3D heterogeneous subsurface structures and typical 3D data acquisition geometries, which are usually employed in practice. Because the implementation of 3D elastic FWI is still computationally challenging, studies on its realization and application and on the elaboration of optimal algorithms as performed by Epanomeritakis *et al*. (2008), Castellanos *et al*. (2011), Guasch *et al*. (2012), Butzer, Kurzmann and Bohlen (2013) are questions of present interest.

Generally, the elastic FWI problem in the Fourier domain is defined as a regularised weighted least squares optimisation problem (Pratt, Shin and Hicks 1998; Pratt 1999; Sirgue and Pratt 2004; Shin and Cha 2009). The transformation from 2D to 3D geometry not only dramatically increases the amount of unknown attributes, which dictate the amount of computations required, but also simultaneously increases the complexity of the objective function, exacerbating well-known local minima problems that arise in nonlinear optimisation (Lasdon 1970; Gill, Murray and Wright 1981; Bjorck 1996; Forst and Hoffmann 2010; Bühlmann and van de Geer 2011). Moreover, increases in the data volume necessary for 3D FWI may not lead to the improvement of image resolution but rather to additional problems with local minima realisations (Perel'man 1981), resulting from severe cycle skipping. Using different kinds of objective functions (Shin and Min 2006; Shin and Ha 2008) may prevent, but does not resolve, this problem. The presence of a large number of local extrema causes difficulty in the application of the gradient method (Pratt *et al*. 1998; Sirgue and Pratt 2004; Shin and Cha 2009) because of the small radius of convergence (Maine and Iliff 1981). Using a good starting model can resolve this issue and essentially reduce the amount of computations; however, in practice, such model is rarely available.

Currently, the preferred approach for treating a local minima problem is to work with datasets having low-frequency content (Bunks *et al*. 1995; Pratt 1999), provided that the data described by such frequencies possess sufficient accuracy. Particularly for onshore datasets, the common scheme for FWI has been to use datasets with relatively large offsets (typically 8 km or more)

and frequencies as low as 2.8 Hz (Ben-Hadj-Ali, Operto and Virieux 2008; Wang and Rao 2009; Wang, de Hoop and Xia 2012; Vigh *et al*. 2011, 2013) or Laplace-domain waveform inversion, which technically corresponds to zero frequency (Ha and Shin 2012). Although the implementation of low-frequency data can help avoid the local minima problem in some cases, it still has issues with recovering velocities in the deeper part of the model (Operto *et al*. 2013; Ren and Liu 2016) and requires a starting model very close to an acceptable model. As a simple rule, starting models without *a priori* information lead to local minimum realisation. Note that most 3D FWI papers use a smoothed model of the expected solution as starting models and do not discuss the local minima problem when starting models are far from the expected solution. In this paper, we propose a multistep workflow for 3D elastic FWI using laddered offset data in the damped Fourier domain, which can 1) reduce local minima realisations, 2) efficiently recover the deep part of a velocity model, and 3) provide robust convergence of the inversion process to the desired solution without cycle skipping, even if a simple starting model is used. This starting model is not a smoothed version of the expected velocity model and is quite far from the correct solution. Our approach is based on the treatment of different data offsets, which are sensitive to different interrogation depths (Sirgue and Pratt 2004). In contrast to classic FWI in the frequency domain (Pratt 1999; Sirgue and Pratt 2004; Shin and Min 2006), where all data at a specific frequency are used simultaneously and frequencies are changed sequentially from low to high, we propose performing the inversion process sequentially, thereby increasing offsets to maximum aperture, together with cyclical sampling of frequency and damping constants. For each fixed offset, the Fourier frequencies are changed sequentially from low to high and the Laplace damping constants from large to small. When changing offset lengths to larger ones, the inversion begins anew from the lowest frequency and with larger damping. Only at the terminal stages of the FWI process are all the data comprising the longest offsets employed. Additionally, as a final step, a reverse loop is used when, after inversion at the highest frequency, we return to the lowest frequency and repeat the process with minimal damping.

The goal of this paper is to demonstrate that a multistep workflow can treat long-offset data for realistic synthetic examples at a resolution consistent with the inverted frequencies. Here, we describe the application of the algorithm and multiscale strategy to reconstruct the elastic attributes of the Marmousi-2 model (Martin, Marfurt and Larsen 2002; Xiong *et al*. 2013) with offsets up to 9 km and the SEG/EAEG Salt model (Aminzadeh, Brac and Kunz 1997) with offsets up to 13 km.

METHOD OF ELASTIC WAVEFORM INVERSION

Following the inverse problem formulation in the frequency domain (Pratt 1999; Sirgue and Pratt 2004) and its extension in the Laplace–Fourier domain for acoustic problems (Shin and Cha 2009), we define the elastic full-waveform inversion problem as determining an elastic attribute model $\mathbf{m} = (b, \kappa, \mu)$ (bulk and shear moduli κ, μ and buoyancy $b = 1/\rho$, where ρ is the mass density), which minimises an objective functional expressed by the residuals between the model responses and the observed data $\phi_d(\mathbf{m})$ with a model smoothness constraint $\phi_R(\mathbf{m})$. Specifically, we write:

$$\begin{aligned}\phi(\mathbf{m}) &= \phi_d(\mathbf{m}) + \phi_R(\mathbf{m}),\\ \phi_d(\mathbf{m}) &= \frac{1}{2}\sum_q \left(\mathbf{d}_q^{obs}(s_q) - \mathbf{d}_q^{sim}(\mathbf{m}, s_q)\right)^H \mathbf{E}^H \mathbf{E} \left(\mathbf{d}_q^{obs}(s_q)\right.\\ &\quad \left. - \mathbf{d}_q^{sim}(\mathbf{m}, s_q)\right),\\ \phi_R(\mathbf{m}) &= \frac{1}{2}\lambda \mathbf{m}^T \mathbf{W}^T \mathbf{W}\mathbf{m}.\end{aligned} \quad (1)$$

In equation 1, $\mathbf{d}_q^{obs}(s_q), \mathbf{d}_q^{sim}(\mathbf{m}, s_q)$ are the observed and predicted data vectors, with subscript *q*indicating the source index; **E** is the diagonal matrix of weights defined by the data error; **W** is the regularisation matrix, which consists of a finite-difference approximation to the gradient operator (∇_m); λ is the regularisation parameter to balance data error and the model smoothness constraint; and symbols "*H*, *T*" denote the Hermitian conjugate and transpose operations, respectively. The observed data vectors consist of the Laplace–Fourier image of elastic displacement velocities, obtained from the measured time-domain seismic wavefield data:

$$\mathbf{d}_q^{obs}(s_q) = \int_0^\infty \mathbf{d}_q^{obs}(t)\, e^{-s_q t} dt, \quad (2)$$

with complex frequency $s_q = \sigma_q + i\omega_q$, where σ_q is the Laplace damping constant, and ω_q is the angular frequency with $i = \sqrt{-1}$.

Predicted data $\mathbf{d}_q^{sim}(\mathbf{m}, s_q) = (d_{q1}^{sim}(\mathbf{m}, s_q), d_{q2}^{sim}(\mathbf{m}, s_q), \ldots)^T$ are defined by the displacement velocity field and depend upon the model parameters **m**

$$\mathbf{d}_q^{sim}(\mathbf{m}, s_q) = \hat{\mathbf{G}}_q \mathbf{v}_q(\mathbf{x}, \mathbf{m}, s_q), \quad (3)$$

where $\hat{\mathbf{G}}_q$ is an interpolation operator applied to the calculated velocity field in the vicinity of the detector positions for the source with index *q*. The velocity components $\mathbf{v}_q(\mathbf{x}, \mathbf{m}, s_q) = (v_{q,x}, v_{q,y}, v_{q,z})$ at the spatial location **x** specified in equation 3 satisfy the system of finite-difference elastic equations (Virieux 1986):

$$\mathbf{K}(b, \kappa, \mu, s_q)\mathbf{v}_q = \mathbf{f}_q, \quad (4)$$

where $\mathbf{f}_q$ is the body forces for the *q*th source, and $\mathbf{K}(b, \kappa, \mu, s_q)$ is a finite-difference operator whose explicit expression can be found in Petrov and Newman (2012, 2014).

We minimise the objective functional in equation 1 using the nonlinear conjugate gradient method (Fletcher and Reeves 1964; Polyak and Ribière 1969; Newman and Alumbaugh 2000; Petrov and Newman 2014) with the pseudo-Hessian matrix as a preconditioner (Choi *et al*. 2008). In addition to preconditioning, the choice of regularisation parameter λ has a pronounced effect upon convergence of the inverse iteration and results. It is used to control the amount of smoothness to be incorporated into the inverse model. Large values of λ will produce very smooth models, at the expense of poorer fits to the observed data. Small parameters give superior data fits, but the resulting models can be nonphysical. Our modelling strategy is to use the largest value of λ, which realises an acceptable match to data within observational errors. Typically, it is selected such that

$$\lambda \nabla_m \phi_R \approx (0.1 \ldots 0.8) \cdot \nabla_m \phi_d, \quad (5)$$

where $\nabla_m \phi_{d,R} = \frac{\partial \phi_{d,R}}{\partial \mathbf{m}} = \left(\frac{\partial \phi_{d,R}}{\partial b}, \frac{\partial \phi_{d,R}}{\partial \kappa}, \frac{\partial \phi_{d,R}}{\partial \mu}\right)$ are the gradients of the data misfit and the model smoothness constraint parts of the objective function defined in equation 1. Evaluation of $\nabla_m \phi_R$ directly leads to

$$\nabla_m \phi_R = \mathbf{W}^T \mathbf{W} \mathbf{m}, \quad (6)$$

and for the data misfit part, we obtain

$$\nabla_m \phi_d = -\sum_q \mathrm{Re} \left\{ \left(\mathbf{d}_q^{obs}(s_q) - \mathbf{d}_q^{sim}(\mathbf{m}, s_q) \right)^H \mathbf{E}^H \mathbf{E} \mathbf{G}_q \nabla_m \mathbf{v}_q(\mathbf{m}) \right\}. \quad (7)$$

The gradient of velocities $\nabla_m(\mathbf{v}_q(\mathbf{m}, s_k))$ may be obtained directly from equation 4 (Petrov and Newman 2014).

STRATEGY OF WAVEFORM INVERSION IN THE LAPLACE–FOURIER DOMAIN

Usually, a sequential single-frequency Fourier-domain waveform inversion approach for imaging across multiple scales is employed as first proposed by Tarantola (1984), Bunks *et al*. (1995), Pratt (1999), and Sirgue and Pratt (2004) and later for the Laplace–Fourier domain by Shin and Cha (2009) and Shin *et al*. (2010) among others. Because the frequency is now complex-valued $s = \sigma + i\omega$, consisting of the Laplace damping factor σ and the angular frequency ω, waveform inversion will involve multiple real-valued frequencies and damping constants. The choices made in selecting these frequencies and damping constants, as well as their respective ordering, are critical for the successful outcome of the inversion experiment. Shin *et al*. (2010) proposed a

workflow wherein frequencies are changed from low to high and Laplace damping constants from large to small. Figure 1a illustrates this waveform inversion scheme. The proposed ordering allows possibilities of decreasing cycle skipping and local minima issues (Virieux and Operto 2009) and employs a multiscale imaging approach (Fichtner 2011), where the functional in equation 1 is smoother at lower than at higher frequencies (Brown, Jais and Knowles 2005). Additionally, starting the inversion process with a large damping constant at a given frequency will result in faster overall solution time than starting with lower damping, owing to the improvement of forward operator spectral properties (Erlangga, Vuik and Oosterlee 2004).

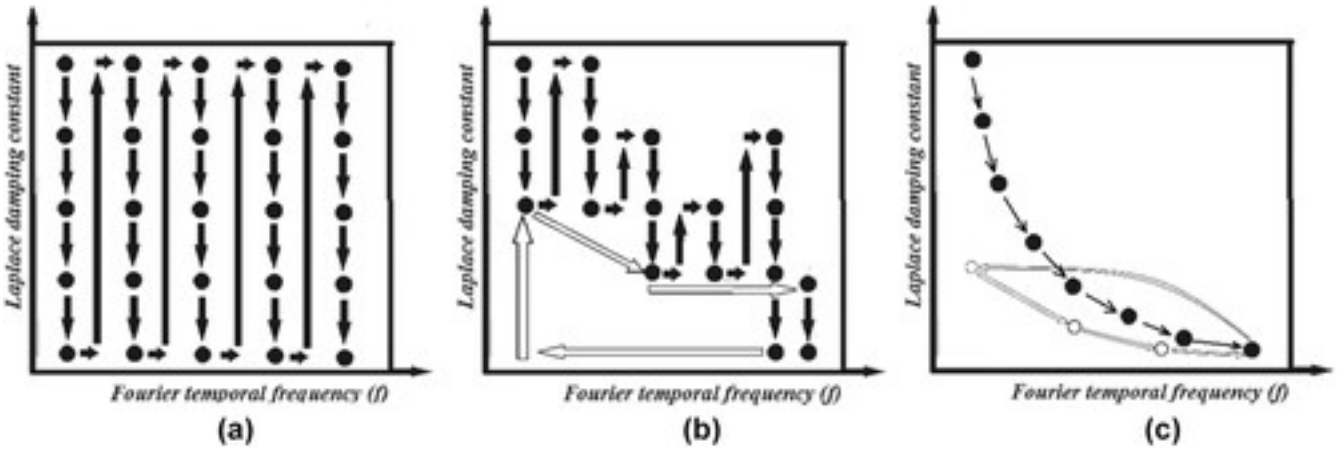

Figure 1
Open in figure viewerPowerPoint
(a) Sequential waveform inversion scheme in the Laplace–Fourier domain. (b) Truncated damping waveform inversion scheme with a reverse loop. (c) Optimal workflow for the waveform inversion scheme in the Laplace–Fourier domain with a reverse loop.
Caption

However, such order of inversion (Fig. 1a) may not be necessarily optimal, because the implementation of large damping, proceeding from low to high frequencies, will smooth out specific structures in the image, which were obtained with a small damping constant during the previous inversion cycle. Thus, it seems more practical not to cover the full range of damping constants at lower frequencies, but rather to truncate them to insure that the image resolution will be similar to that obtained with the largest damping constant employed at the next frequency. Additionally, the final solution of the inverse problem must satisfy all complex frequencies employed in the imaging experiment independent of the strategy employed. Thus, after inversion at high frequencies, it is necessary to return to the lower frequencies. The reverse loop helps preserve the content of lower frequency data in the imaging process as data with higher frequency content are added. We propose that the recurrence to lower frequency be made at least one time after the completion of inversion at the highest frequency. Figure 1b presents the truncated cycle with the reverse loop for the waveform inversion. In an optimal limit (ideal case),

a 2D strip of damping constant and frequencies will degenerate to a 1D curve. Hence, for each frequency, it will be necessary to perform only one inversion as shown in Fig. 1c, before executing the reverse loop at the terminal stages of the inversion workflow. The main condition for the optimal relation between damping and frequency is the self-consistency between wavelength and “diffusion” lengths:

$$\lambda^{p,s} = \frac{2\pi \langle V_{p,s} \rangle}{\omega} \sim \lambda_D^{p,s} = \sqrt{\frac{2\pi}{\omega\sigma}} \langle V_{p,s} \rangle, \quad (8)$$

where $\langle V_{p,s} \rangle$ P- and S-wave velocities are averaged over the inversion domain.

Thus, the sequential strategy transforms into a sequentially recursive type (Fig. 1b). We showed in Petrov and Newman (2014) that this strategy, when combined with multiscale imaging in frequency, can be used to great advantage to produce high-resolution 3D images of elastic attributes in a cost-effective manner.

Unfortunately, because of the absence of a very good initial model for full waveform inversion (FWI) with long-offset data, the direct implementation of the standard sequential ordering schemes or the aforementioned sequentially recursive scheme cannot archive an acceptable solution with the desired data misfit. Very often, after a few iterations, the gradient minimisation leads to a local minimum of error functional, where the data error misfit is far above its target value. The possible reason is that the short- and long-offset data give conflicting gradient search directions for the applied initial model. The inability to match the experimental data for the full set of receiver data leads to a slowdown in convergence of the inversion iteration and, finally, to local minima realisation.

To avoid this problem, we have to resolve the contradiction between the different data offsets. The obvious solution is to perform FWI with the sequentially increasing offsets, because for the smaller offsets, the probability of cycle skipping is less, the convergence rate is higher, and small data errors are possible. Increasing offset leads to increasing the depth of the illuminated region; hence, we may consider this strategy as sequentially increasing the depth of the inverted image. While the transition to multistep FWI with laddering offsets makes inversion more computationally expensive, the strategy makes it more robust to the starting model and significantly aids in eliminating the local minima problem.

Two different approaches can be realised in the workflow for sequentially increasing offsets where all data within a fixed offset are used. The first approach involves sequentially utilising FWI over complex frequencies for each fixed offset, in which the result of inversion is then used as the starting model for the next larger offset (Fig. 2a,b). In the second approach (not

illustrated), offsets are increased up to their maximum at each and every frequency. Both approaches include periodic reverse loops (Petrov and Newman 2014). We have tested both of these approaches with obtaining approximately the same results and similar computer time expense. Each approach demonstrated the desired robustness for treating long-offset data. In our opinion, the first approach (Fig. 2a,b) is preferable because it allows more visual control of the result after each offset inversion and requires only one explicit reverse loop; starting inversion for the next larger offset from the lowest frequency is an implicit reverse loop. The optimal workflow can be visualised as a spiral curve in 3D space $(f, \sigma, offset)$ and is illustrated in Fig. 2c.

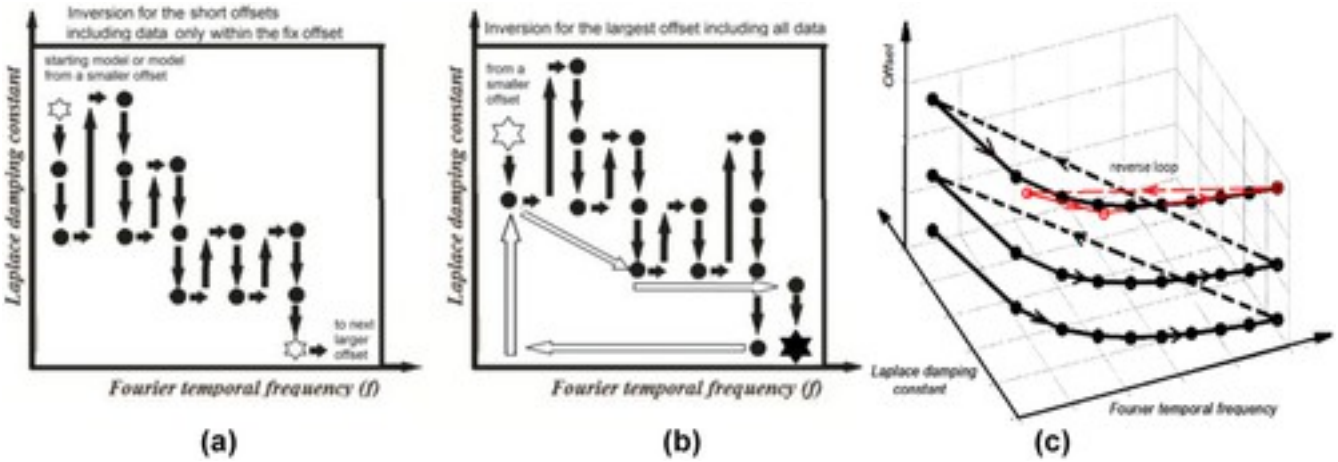

Figure 2
Open in figure viewerPowerPoint
(a) Sequential waveform inversion in the Laplace–Fourier domain for shorter offsets. (b) Final waveform inversion with the reverse loop for the longest offset, which includes all data. (c) Optimal sequentially recursive strategy for inversion with offset.
Caption

SYNTHETIC EXAMPLES

Marmousi model

In this example, we apply our 3D full waveform inversion (FWI) workflow to the Marmousi-2 elastic model, which is invariant along its strike direction, denoted by the *y*-axis. In Fig. 3a,b, P- and S-wave velocities are given. In comparison with the model described by Martin *et al*. (2002), the low S-wave velocity was increased up to 1000 m/s as used in Xiong *et al*. (2013). The dimension of the inversion domain is 9.2 × 3.2 × 4.0 km, and it is discretised into 191 × 66 × 70 grid cells with the grid spacing of 48 m. Synthetic data were generated by the Laplace–Fourier-domain finite-difference modelling technique where a free-surface boundary condition was imposed on the water surface, and on the other boundaries, the perfectly matched layer (PML)

absorbing condition was applied (Petrov and Newman 2012). Note that the density is defined by the Gardner relation (Gardner, Gardner and Gregory 1974):

$$\rho = AV_p^{1/4}, \quad (9)$$

where A = 284 when the data from the model are inverted. For the exact model, A changes with depth from 280 to 295.

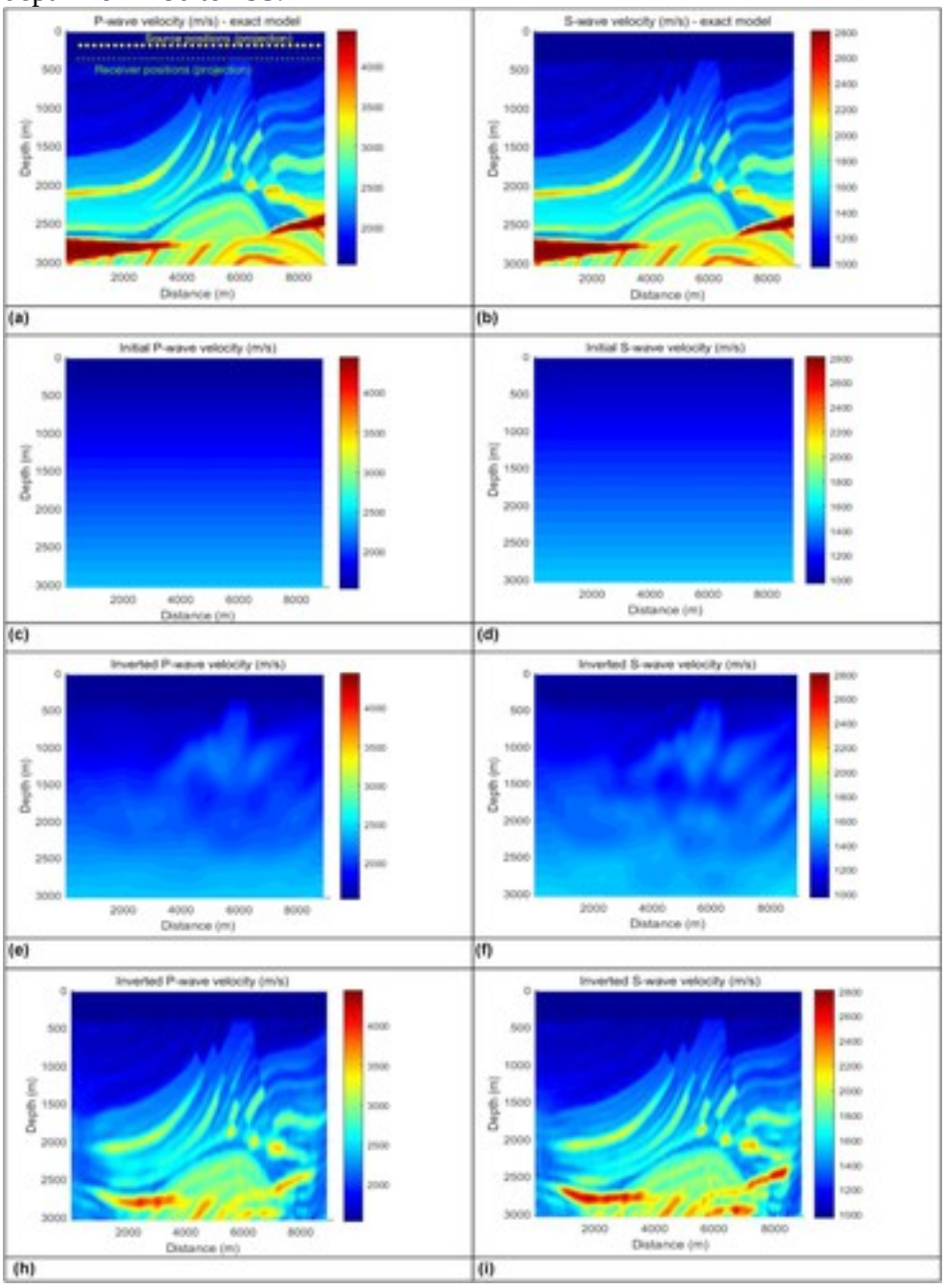

Figure 3

Open in figure viewerPowerPoint

(a and b) True model, (c and d) starting model, and (e and f) the corresponding inverted model based upon full offset data without the multistep offset strategy and (h and i) final results with the multistep strategy after 6-Hz data inversion for the P- and S-wave velocities (m/s) of the Marmousi-2 elastic model.

Caption

There are 396 dipole point sources uniformly located from x = 432 m to x = 8320 m, along 11 lines that span y = –1200 m to y = +1200 m at 240-m intervals, and at the depth of 192 m. A total of 2403 receiver locations are equally spaced from x = 360 m to x = 8808 m, along with 27 lines that span y = –1248 m to y = +1248 m at 96-m intervals; the inline y = 0 measures two components per detector (x and z components of the velocity displacement field), whereas the broadside lines have three components per detector (x, y, and z components of the velocity displacement field). The receiver depth is 360 m. A projection of the geometry of survey is presented in Fig. 3a. At the longest offsets, each source uses all available receivers, where weights in equation 1 are proportional to the absolute value of the observed velocity field, i.e., $\mathbf{E}_{cl} \sim |\mathbf{d}^{obs}|$, to compensate for attenuation and geometric spreading of the observed data with offset. The distribution of observed data along the x-axis offset for the shot placed at the point (x = 432 m, y = 0 m, z = 192 m) is shown in Fig. 4a,b at 6 Hz for a specific broadside profile. The inverted model responses are based upon the multistep inversion strategy illustrated in Fig. 5a,b.

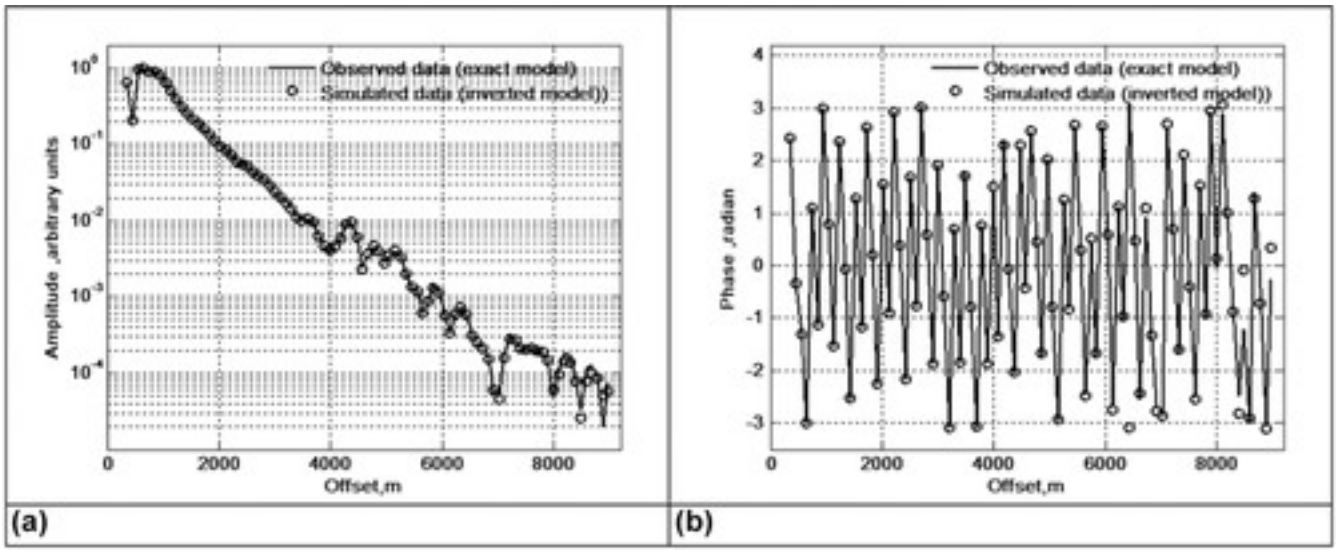

Figure 4

Open in figure viewerPowerPoint

Observed and simulated data are shown for the exact and inverted Marmousi-2 elastic model at the frequency of 6 Hz with damping constant 1 s^{-1}. (a) Amplitude and (b) phase of the V_z data component.

Caption

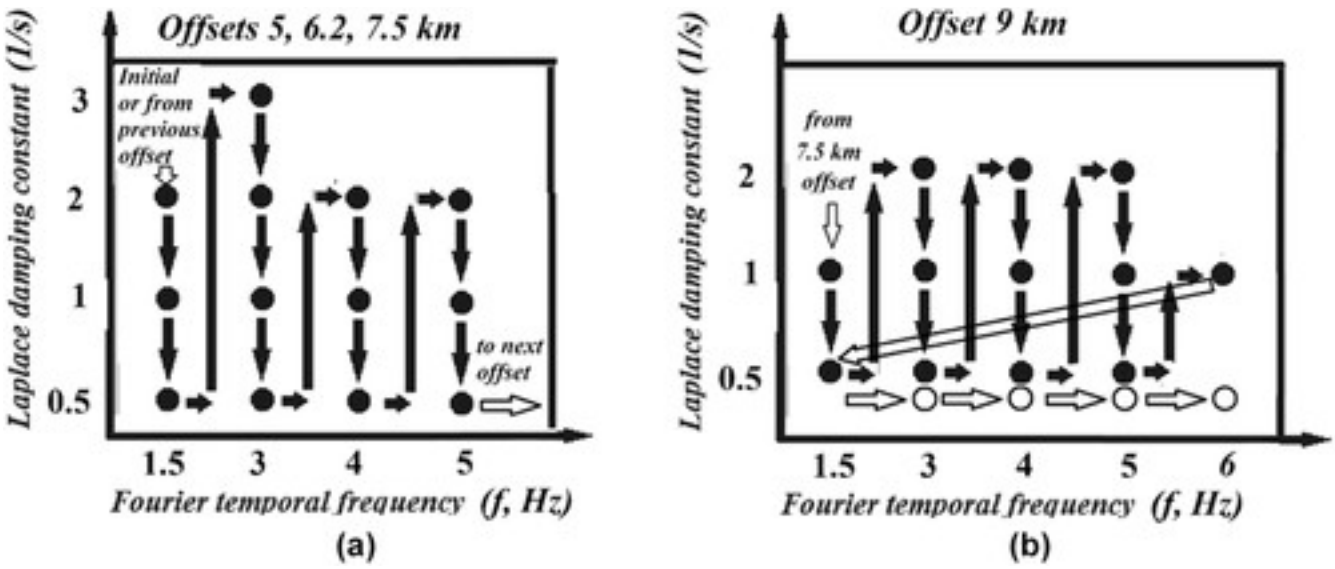

Figure 5

Open in figure viewerPowerPoint

(a) The waveform inversion workflow for the Marmousi-2 model in the Laplace–Fourier domain uses sequentially increasing offsets 5, 6.2, and 7.5 km, (b) with the offset of 9 km including the reverse loop with the smallest damping constant (0.5 s^{-1}).

Caption

We use a normalised percentage data error e_n for assessing the quality of the data fits in the results that follow. Specifically, we have

$$e_n = \frac{1}{N_q}\sqrt{\sum_q \frac{\Delta \mathbf{d}_q{}^H \Delta \mathbf{d}_q}{\left(\mathbf{d}_q^{obs}\right)^H \mathbf{d}_q^{obs}}} \times 100\%. \quad (10)$$

Here, N_q is the total number of sources for different source positions with distinct Laplace–Fourier damping/frequency parameters.

The data are inverted with five different frequency sets, which include 1.5, 3, 4, 5, and 6 Hz, such that there are at least five grid points per wavelength for the shear wave at 6 Hz. The initial velocity model is composed of linearly increasing velocity functions with depth, with P-wave velocity varying from 1500 to 2500 m/s and S-wave velocity varying from 1000 to 1600 m/s (Fig. 3c,d).

At first, we attempted to realise the FWI inversion with a full dataset; each source used all receiver data with a maximum offset of 9 km. The single-frequency inversion strategy shown in Fig. 1b was realised (Petrov and Newman 2014) when frequencies were sequentially changed from the lowest (1.5 Hz) to the highest (6 Hz) and damping constants from the largest (3 1/s) to the smallest (0.5 1/s). Unfortunately, with long-offset data, we could not achieve an acceptable

solution with the desired data misfit (Fig. 3e,f) . The normalised data error e_n obtained was about 40%, which indicated local minimum realisation. Changing the damping and starting with lower frequency data did not have any essential effects on improving the results.

To avoid a local minimum, we resorted to the multistep workflow using sequentially increasing offsets 5, 6.2, 7.5, and 9 km at frequencies of 1.5, 3, 4, 5, and 6 Hz with damping constants 3, 2, 1, and 0.5 1/s. For each source, all receiver data within the fixed offset were used. Implementing offsets less than 5 km makes no sense because at each inversion step, we observe good convergence for all frequencies and no issues with local minima realisation. In this case, inversion with the smaller offsets leads only to additional expenditure of computer time. The inversion workflow is shown in Fig. 5a,b. Changes in P- and S-wave velocities inverted for different offsets at 3 Hz can be observed in Fig. 6, which clearly manifests how offset laddering improves image quality with depth. Having realised the inversion with the largest offset, we made the reverse loop beginning with the lowest frequency of 1.5 Hz and then with 3, 5, and 6 Hz with the same damping constant 0.5 (1/s). The final results from the inversion workflow (Fig. 5) are shown in Fig. 3h,i and Figs. 4, 7, and 8. As shown in the figures, the inversion gives very good results down to 3 km in depth, with a high spatial resolution defined by the highest frequencies, i.e., 5–6 Hz. Some regions on the left- and right-hand sides of the images are not well rendered, resulting from the limited size of the source–receiver aperture in the measurement array. The data misfit e_n over the full offset of 9 km is less than 4%.

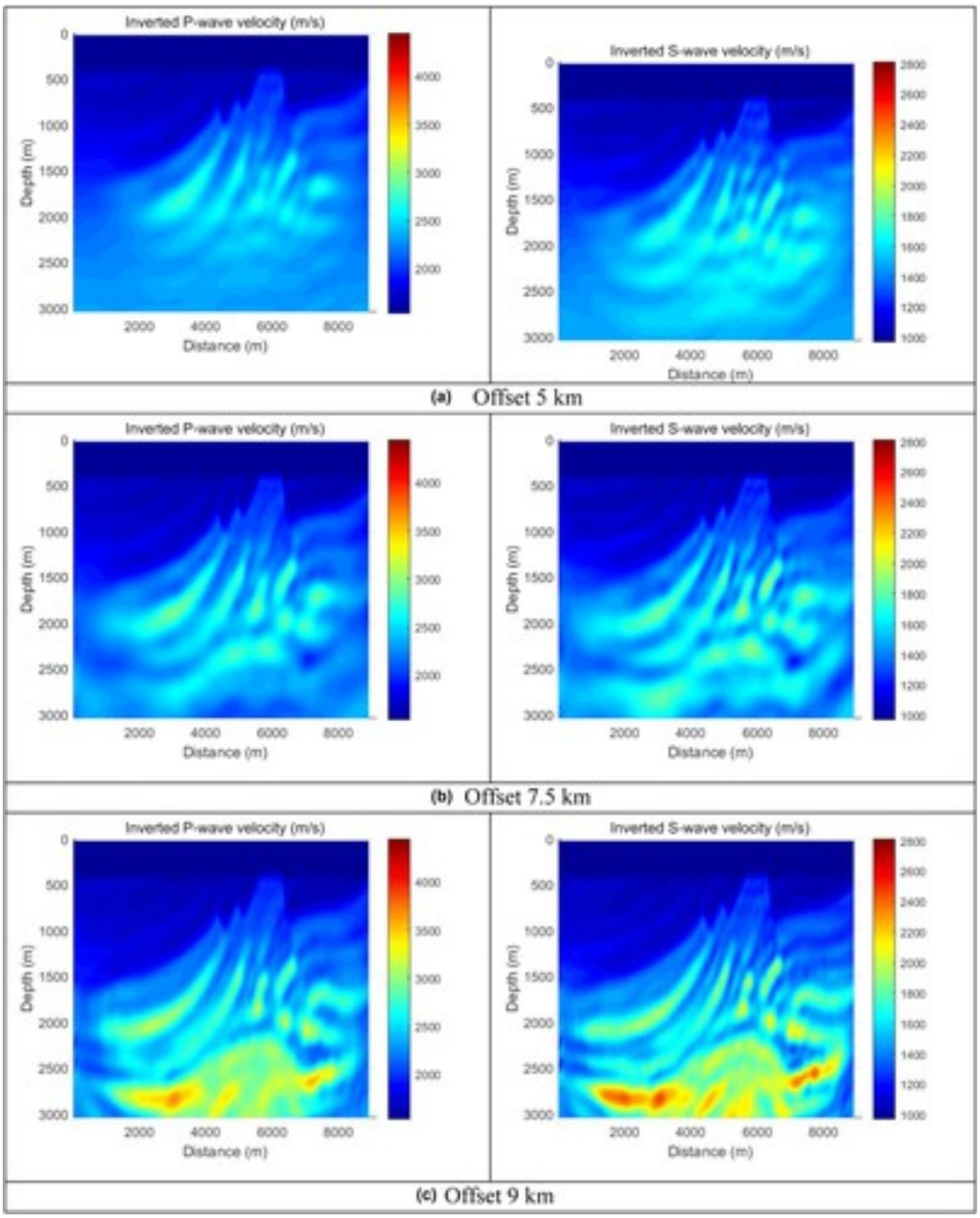

Figure 6

Open in figure viewerPowerPoint

The intermediate inversion results for the P- and S-wave velocities (m/s) of the Marmousi-2 model for the different offsets (a) 5, (b) 7.5, and (c) 9 km at the frequency of 3 Hz and the damping constant of 0.5 (1/s) (see Fig. 5a).

Caption

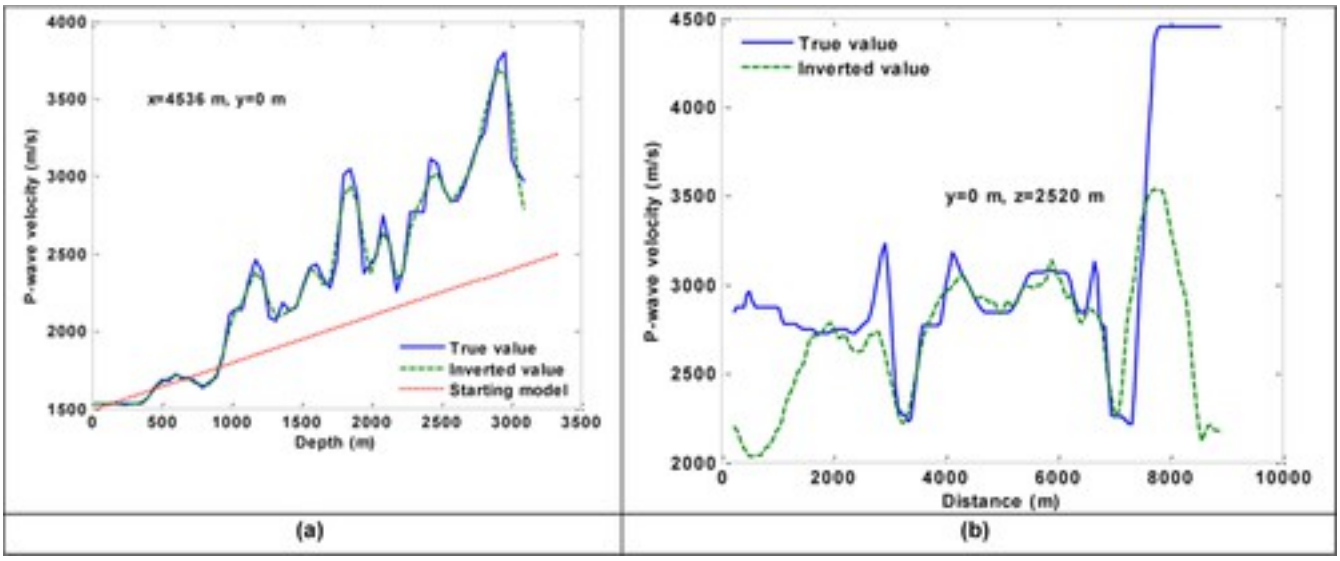

Figure 7

Open in figure viewerPowerPoint

(a) Vertical and (b) horizontal P-wave velocity profiles for the true, inverted, and initial models.

Caption

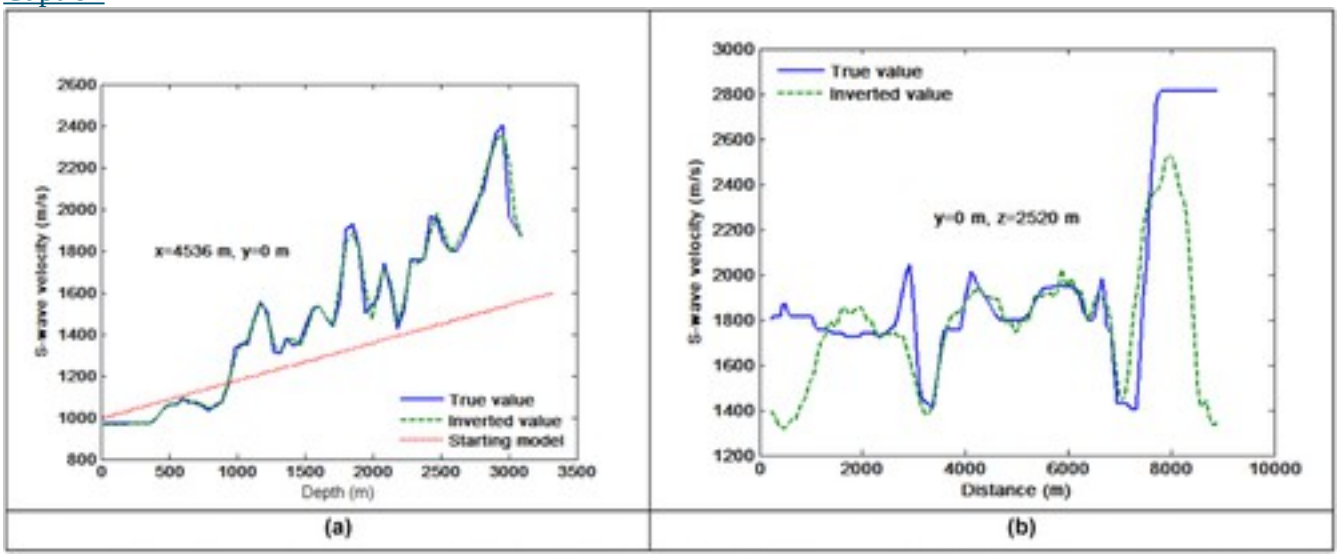

Figure 8

Open in figure viewerPowerPoint

(a) Vertical and (b) horizontal S-wave velocity profiles for the true, inverted, and initial models.

Caption

In our workflow, we pay special attention to reverse loops, which make results essentially better. Figure 9 presents the results of the inversion without any reverse loops for comparison with Fig. 3h,i. We observe that below 2.5 km in depth, the recovered images correspond only fragmentarily to the correct solution and do not reproduce complex structures, although the data misfit e_n is less than 6%.

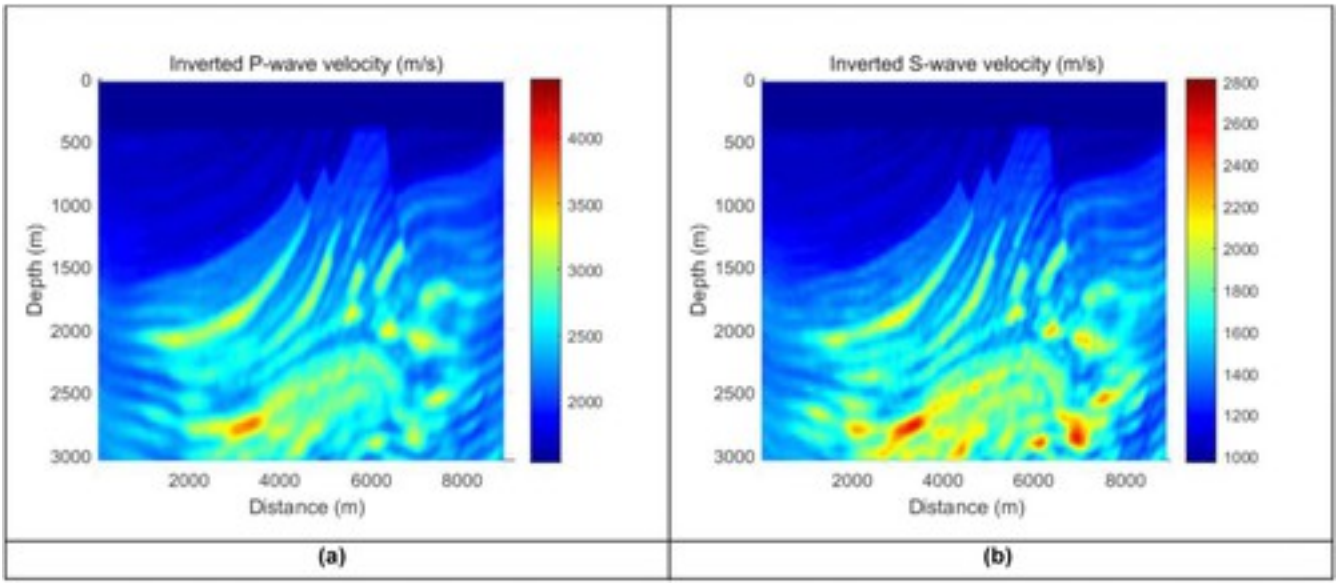

Figure 9

Open in figure viewerPowerPoint

Results of inverting the P- and S-wave velocities (m/s) of the Marmousi-2 elastic model without reverse loops.

Caption

The inversion of the Marmousi model demonstrates that the multistep FWI algorithm, based on sequentially ordered offsets and single-frequency inversion, which efficiently exploits damped wavefields, can successfully image complex 3D structures that are sensitive to long-offset data. The important condition for successful inversion is the reverse-loop implementation, which renews low-frequency components of the solution and performs quality control over all frequencies.

3D SEG/EAGE Salt model

To test the feasibility of the elaborated FWI workflow on a more difficult problem, we consider the 3D SEG/EAGE velocity model (Aminzadeh *et al*. 1997). The parameters of the model are defined by House, Larsen and Bednar (2000), where, similar to the Marmousi model, the low shear wave velocity was increased from 0 to 300 m/s in sea water.

To reduce both the required memory and computing time, we used a part of the SEG/EAGE model $(1800 \le x \le 12250, 1600 \le y \le 11360, \ 0 \le z \le 4520)$ (in meters), which includes the salt body. The distribution of P- and S-wave velocities in the planes $x = 5880$, $y = 5200$, and $z = 2200$ m is shown in Figs. 10a–c and 11a–c, where the number of grid nodes is $155 \times 153 \times 61$ with the grid spacing of 80 m. A free-surface boundary condition was imposed on the water surface. On the other boundaries, the PML condition was applied, with five cells in

each direction. Synthetic data were generated again by the Laplace–Fourier-domain finite-difference modelling technique (Petrov and Newman 2012) using 40-m cell/grid size.

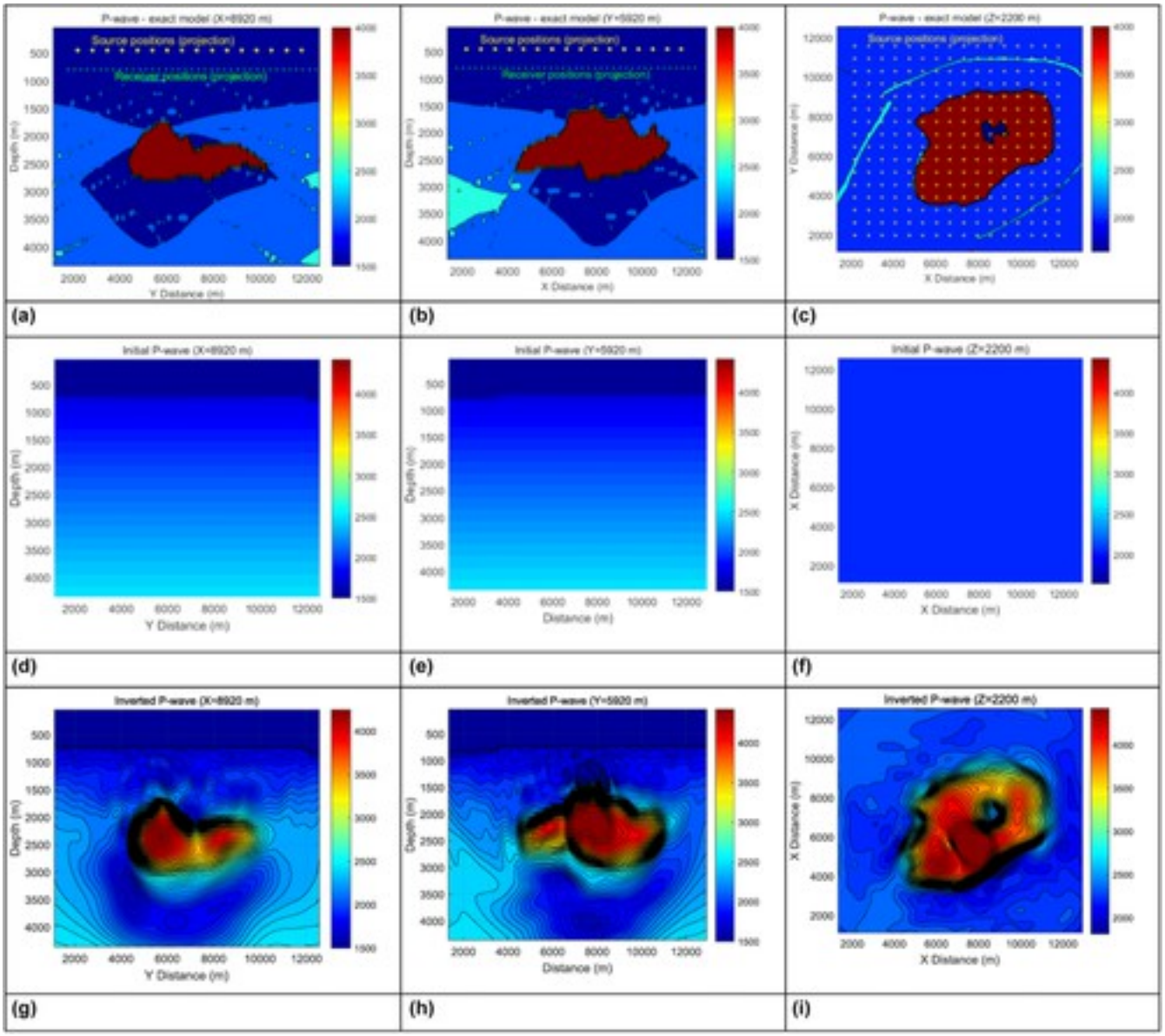

Figure 10

Open in figure viewerPowerPoint

(a–c) True and (d–f) starting models and (g–i) final results after a 2-Hz data inversion for the P-wave velocities (m/s) of the SEG/EAGE Salt elastic model.

Caption

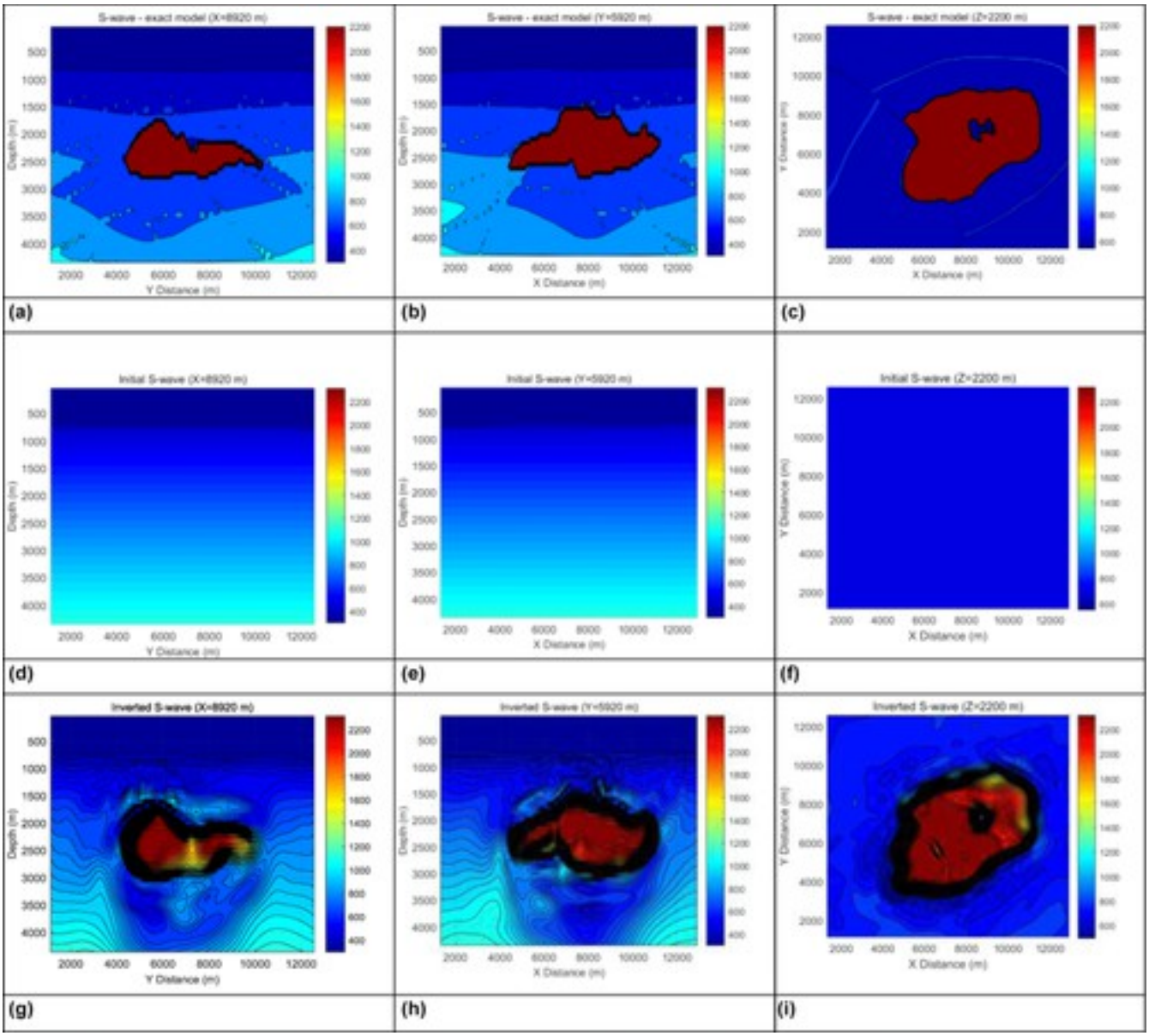

Figure 11

Open in figure viewerPowerPoint

(a–c) True and (d–f) starting models and (g–i) final results after a 2-Hz data inversion for the S-wave velocities (m/s) of the SEG/EAGE Salt elastic model.

Caption

There are 256 pressure point sources uniformly located from x = 2080 m to x = 11 680 m, along 16 lines that span y = 1880 m to y = 11 480 m at 640-m intervals, and at the depth of 480 m. A total of 4624 receiver locations are equally spaced from x = 1480 m to x = 12 200 m, along 68 lines that span y = 1680 m to y = 12 400 m at 160-m intervals; each detector has x, y, and $z$components of the velocity displacement field, where the receiver depth is 720 m. Every source uses all available detectors. The projections of survey geometry are presented in Fig. 10a–

c. Once again, the weights employed in equation 1 are proportional to the absolute value of the observed velocity field ($\mathbf{E}_d \sim |\mathbf{d}^{obs}|$).

The inversion region does not include water layer and begins at sediments from the depth $z \geq z_0 = 840$ m. The density was not inverted. We assumed exact values for density up to the depth of 840 m and linear function dependence at greater depths:

$$\rho = \begin{cases} \rho_{exc}, 0 < z < z_0 \\ \rho_0 + (\rho_e - \rho_0)(z - z_0)/(z_e - z_0), z_0 < z < z_e = 4520\ m, \end{cases} \quad (11)$$

where $\rho_0 = 1100$, $\rho_e = 1400\ (\mathrm{kg/m^3})$. This profile is close to the density of sediments without salt body. The initial velocity model is composed of linearly increasing functions with depth ($z > z_0$), with P-wave velocity varying from 1600 to 2600 m/s and S-wave velocity varying from 450 to 1200 m/s (Figs. 10d–f and 11d–f).

The data are inverted with five different frequencies, which include 0.25, 0.5, 1, 1.5, and 2 Hz with damping constants 3, 2, 1, and 0.5 (1/s), such that there are about five grid points per wavelength for the average shear wave at 2 Hz. At the beginning, the FWI inversion with a full dataset was performed, where, for each source, all receiver data with the maximum offset of 12 km were used. A single-frequency inversion strategy was realised with frequencies ranging from the lowest to the highest and damping constants from the largest to the smallest. As with the Marmousi model, the FWI results employing only long-offset data lead to an unsuccessful outcome and to the realisation of a local minimum. The resulting image showed only slight differences from the starting model at shallow depths. We could not achieve an acceptable data misfit (Fig. 12), where the normalised data error e_n converged to 45%. Decreasing damping and increasing frequency did not have any beneficial effects on the final model.

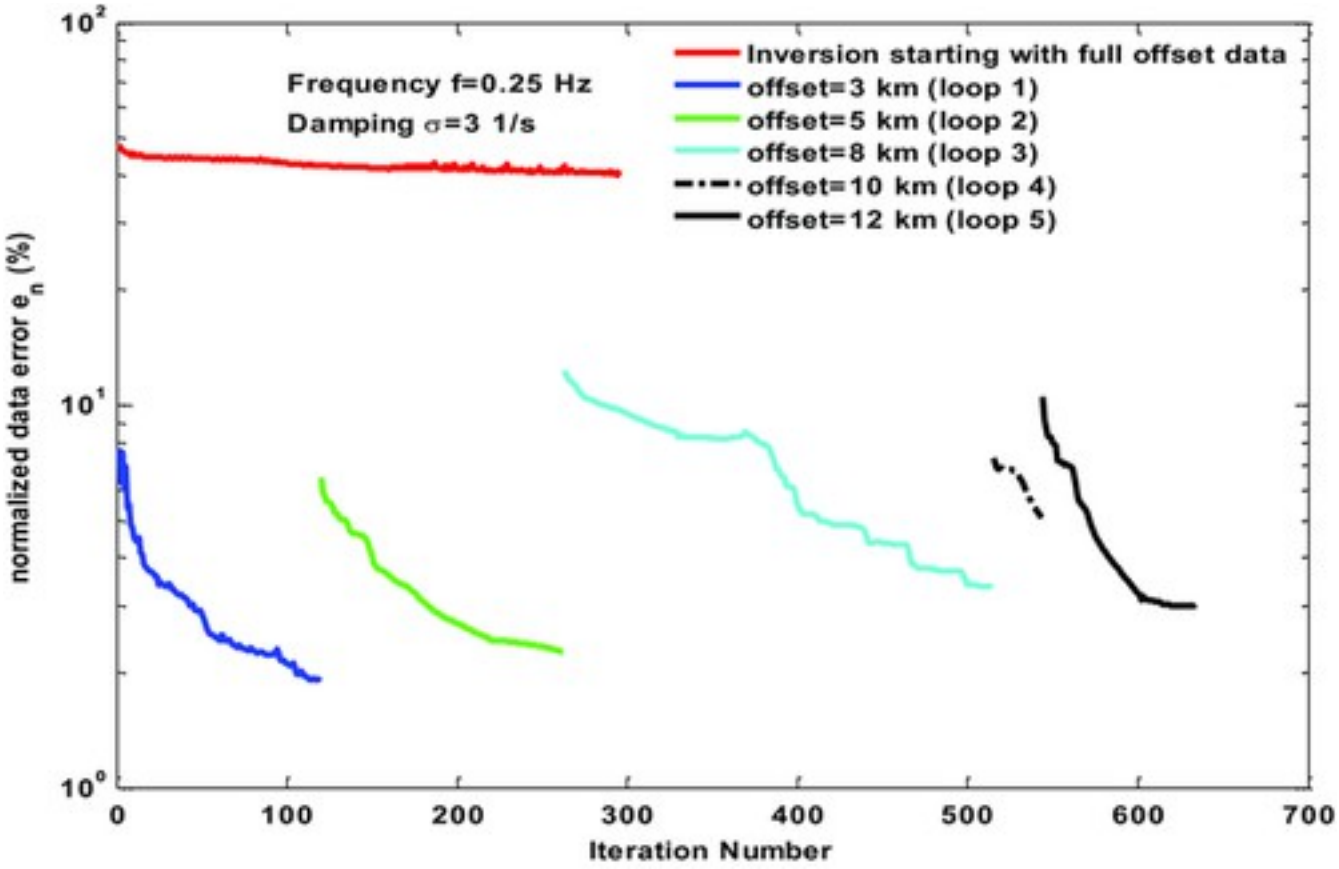

Figure 12

Open in figure viewerPowerPoint

Dependence of the data misfit (%) from the iteration number for inversion with full offset data (12 km) and for multistep inversion with laddered offsets from 3 to 12 km at the frequency of 0.25 Hz and the damping constant of 3 1/s.

Caption

Then, we used the proposed multistep workflow, with sequentially increasing offsets 3, 5, 8, 10, and 12 km at frequencies of 0.25, 0.5, 1, 1.5, and 2 Hz with damping constants 3, 2, and 1 (1/s). The workflow is presented in Fig. 13. At small offsets (3–8 km) with large damping constants 3 and 2 (1/s), the data misfits were less than 6%; at the largest offsets (10 and 12 km) with damping constant 1 (1/s), the data misfits were less than 12%. Figure 12 illustrates the convergence process for the multistep strategy at the frequency of 0.25 (Hz) and the damping constant of 3 (1/s) with laddered offsets from 3 to 12 km. For each offset, the data misfit is very good, indicating avoidance of local minima. The evolution of the inverted P-wave distribution for different offsets at the depth of z = 2040 m is presented in Fig. 14. It is clear that sequentially increasing offsets leads to the reconstruction of a sharper image at a fixed depth and implies increasing resolution with depth.

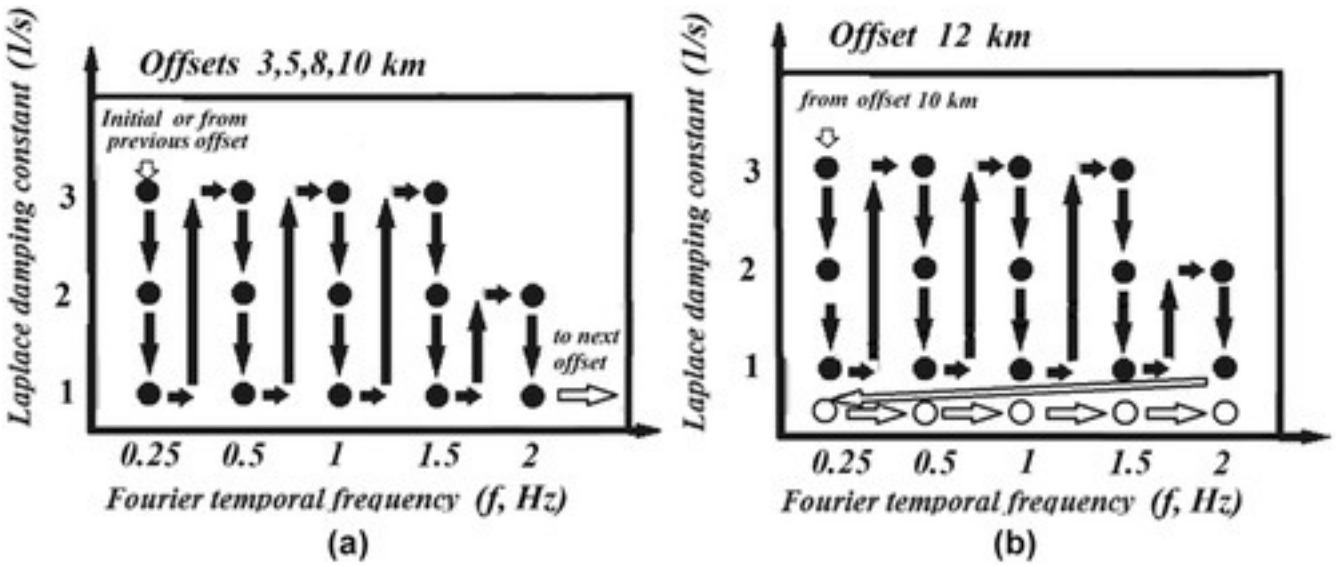

Figure 13

[Open in figure viewerPowerPoint]

(a) The waveform inversion workflow for the SEG/EAGE Salt elastic model in the Laplace–Fourier domain uses sequentially increasing offsets 3, 5, 8, and 10 km, (b) with the offset of 12 km including the reverse loop with the smallest damping constant (1 s^{-1}) at the last stage of the inversion process.

Caption

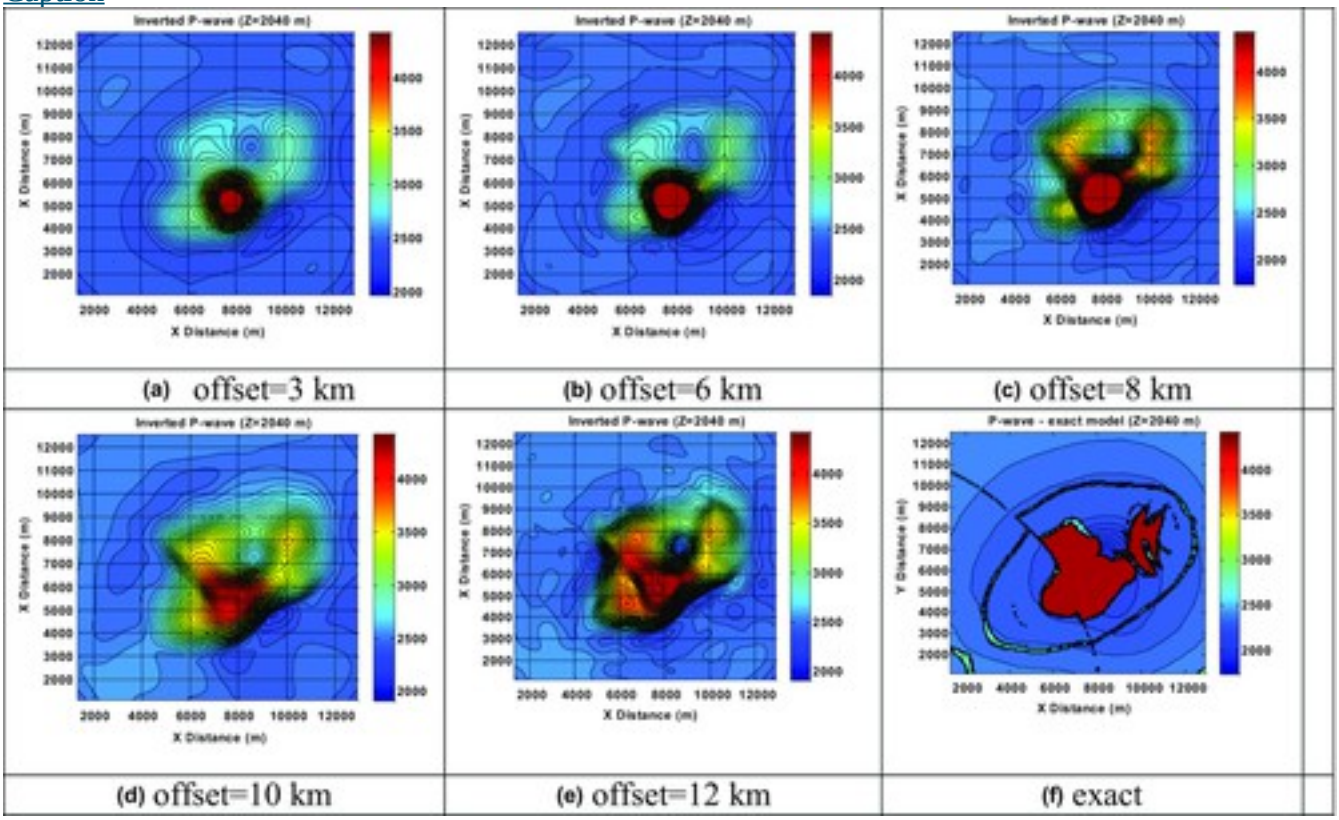

Figure 14

[Open in figure viewerPowerPoint]

(a–e) Inverted and (f) true P-wave velocities (m/s) for the SEG/EAGE Salt elastic model at the depth of z = 2040 m for different offsets at the frequency of 0.25 Hz and the damping constant of 3 (1/s).

Caption

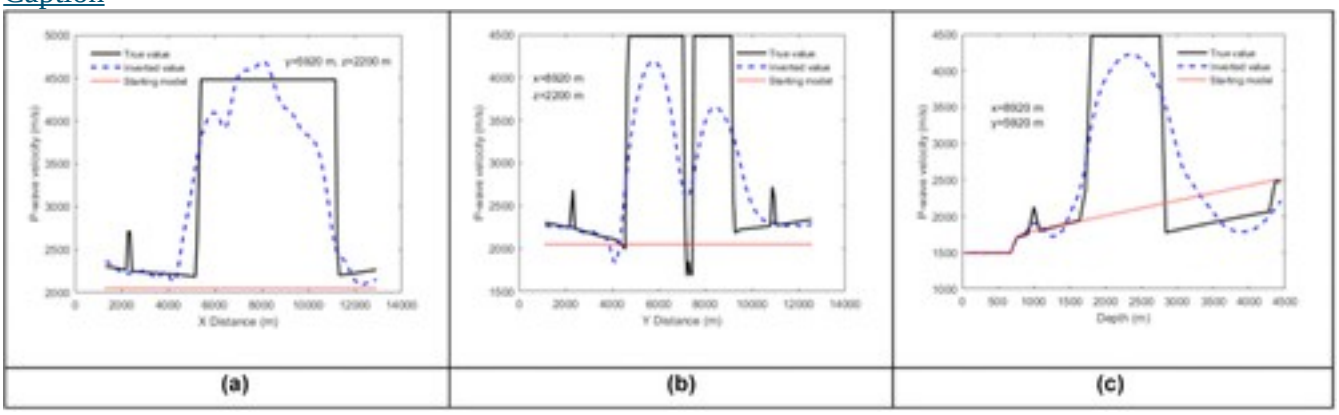

Figure 15

Open in figure viewerPowerPoint

P-wave velocity profiles along the (a) x-, (b) y-, and (c) z-axes for the true, inverted, and initial models.

Caption

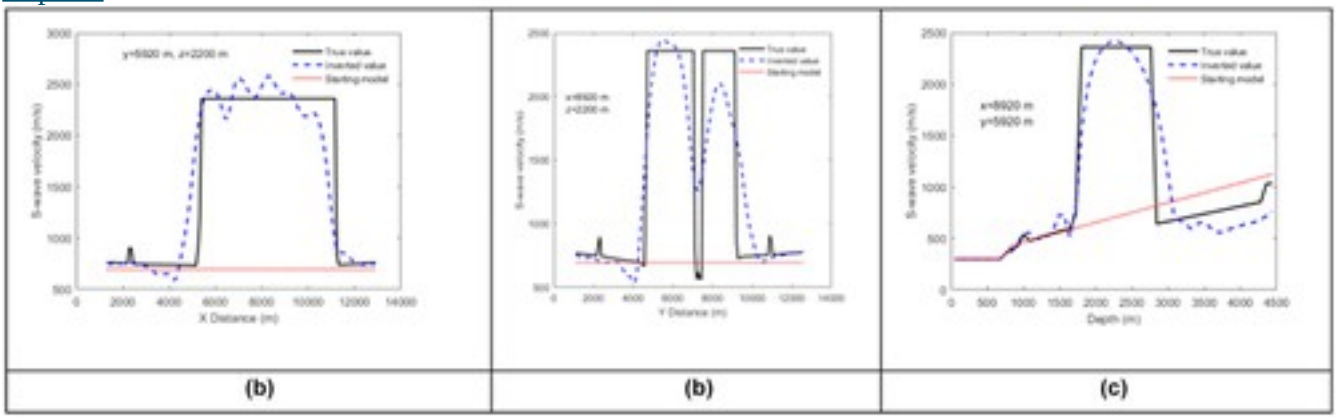

Figure 16

Open in figure viewerPowerPoint

S-wave velocity profiles along the (a) x-, (b) y-, and (c) z-axes for the true, inverted, and initial models.

Caption

The best inversion results for the salt model are shown in Figs. 10g–i, 11g–i, 15, and 16. As shown in the figures, the inversion gives very good results down to 3.5 km in depth. The data misfit e_n over the full offset range of 12 km is less than 12%.

The inversion of the SEG/EAGE Salt model also confirms that the multistep inversion strategy, based on sequentially ordered offsets and cycled frequencies, can successfully avoid local minima and produce 3D images of complex salt structures sensitive to long-offset data.

CONCLUSION

We have proposed a new multistep strategy for an efficient 3D elastic full-waveform inversion (FWI) in the damped Fourier domain using wide-aperture seismic data. The strategy is based on sequential inversion data with increased offset length and frequency cycling. The implementation of the strategy was studied for the 3D inversion of the Marmousi-2 and SEG/EAGE Salt elastic models.

By iteratively inverting from small to large offsets, discrete frequency content from low to high values, and damping constants from large to small, a multiscale imaging scheme is realised, which is sensitive to long source–receiver offsets. High wavenumbers are progressively incorporated into the velocity model, revealing geological features corresponding to the deepest parts of the model. As an inseparable part of the inversion process, we consider and advocate the regular implementation of reverse loops after inversion at one of the highest frequencies. The inversion process is then repeated using lower frequency data, which is needed to preserve the long spatial wavelengths of the recovered velocity models. Such an operation avoids local minima and cycle-skipping artefacts. It guarantees model adequacy at all frequencies. As a result, the inverted velocity model contains a broad and continuous spectrum of wavelengths.

Our results suggest that multistep FWI, with long-offset data and a simple starting model exploiting damped wavefields, can be applied successfully for the inversion of complex subsurface models. The results also show that it is possible to perform accurate 3D velocity imaging down to depths approximately equal to one-third of the maximum offset length and at the resolution that approaches half the smallest wavelength utilised from the data. Finally, while consideration of real data examples was outside the scope of the present paper, we will consider such data in subsequent work.

ACKNOWLEDGEMENTS

This work was supported by the U.S. Department of Energy Office of Science and Office of Energy Efficiency and Renewable Energy (EERE) Geothermal Technologies Program under Grant DE-AC02-05CH11231 and Grant GT-480010-19823-10, respectively. The authors would like to thank the National Energy Research Scientific Computing (NERSC) Center for providing computational resources. All simulations were performed on the NERSC CRAY XE6 and CRAY XC30 supercomputers.